uc3m | Universidad Carlos III de Madrid

e-Archivo

This is a postprint version of the following published document:

Moreno-Boza, D., Coenen, W., Carpio, J., Sánchez, A. L. & Williams, F. A. (2018). On the critical conditions for pool-fire puffing. *Combustion and Flame*, vol. 192, pp. 426–438.

DOI: 10.1016/j.combustflame.2018.02.011

© 2018 The Combustion Institute. Published by Elsevier Inc. All rights reserved.

This work is licensed under a Creative Commons Attribution-NonCommercial-NoDerivatives 4.0 International License.

Combustion and Flame xxx (2018) xxx–xxx

Contents lists available at ScienceDirect

Combustion and Flame

journal homepage: www.elsevier.com/locate/combustflame

On the critical conditions for pool-fire puffing

Daniel Moreno-Boza[a], Wilfried Coenen[a,*], Jaime Carpio[b], Antonio L. Sánchez[a], Forman A. Williams[a]

[a] Department of Mechanical and Aerospace Engineering, University of California San Diego, La Jolla, CA 92093-0411, USA
[b] ETSI Industriales, Universidad Politécnica de Madrid, Madrid 28006, Spain

ARTICLE INFO

Article history:
Received 21 December 2017
Revised 12 February 2018
Accepted 13 February 2018
Available online xxx

Keywords:
Liquid pool fires
Laminar reacting flows
Buoyancy-driven instability,

ABSTRACT

Pool fires are known to undergo a bifurcation to a globally unstable puffing state driven by baroclinic and buoyant vorticity production. Although the supercritical puffing regime away from the bifurcation has been studied extensively in the literature, no detailed account has been given of the critical conditions for its onset, that being the purpose of the present paper. For the relevant canonical case of round liquid pools without swirl, aside from the inherent thermochemical and transport parameters associated with the fuel, pool-fire puffing is governed by a single dimensionless number, the Rayleigh number, which scales with the cube of the pool diameter. Consequently, for a fixed fuel and under fixed ambient conditions, there is a critical fuel pool diameter, associated with a critical value of the Rayleigh number, above which the flame starts puffing. A global linear stability analysis that accounts for the axisymmetry of the prevailing instability mode is developed here to describe the bifurcation. The mathematical formulation employs the limit of infinitely fast reaction, with account taken of the nonunity Lewis number and vaporization characteristics of typical liquid fuels. Predictions of critical puffing conditions, including critical diameters and puffing frequencies, are provided for methanol and for heptane pool fires, and the results are compared with results of new small-scale experiments under controlled laboratory conditions, reported here, yielding reasonably good agreement.

© 2018 The Combustion Institute. Published by Elsevier Inc. All rights reserved.

1. Introduction

Pool fires are known to exhibit a self-sustained oscillatory behavior, shedding large toroidal coherent structures at a well-established frequency, a phenomenon referred to in the literature as "puffing". This behavior influences the rate of air entrainment, soot production, and radiant heat output [1]. Puffing has also been observed to play an important role in flame and wildfire spreading [2,3]. Pool-fire puffing has been studied extensively in the literature, by means of experiments [4–13], numerical simulations [14–20], and scale modeling [21–25]. Extensive reviews on pool fires can be found in [26–29].

It is well established that, under normal conditions of temperature and pressure, diffusion flames formed over hydrocarbon fuel pools larger than a few centimeters in diameter puff with a frequency on the order of 10 Hz, and that this frequency is proportional to the inverse square root of the pool radius a^* according to $f^* \sim \sqrt{g^*/a^*}$, a scaling law that follows from the balance between the unsteady, convective, and buoyancy terms in the Navier–Stokes equations, with g^* denoting the gravitational acceleration. Viscous effects may enter as a stabilizing mechanism for small-scale pool fires, but these have been given little attention in the literature. In particular, no detailed account has been given of the critical conditions for the *onset* of puffing.

The physically similar problem of flickering jet diffusion flames has been recently shown [30] to correspond to a hydrodynamic global instability of the flow. Since the resulting instability modes have wavelengths that are comparable to the flame height, stability analyses based on the quasi-parallel approximation give quantitatively poor predictions. To overcome this difficulty, a global stability analysis was used in [30] to characterize the flickering dynamics near the bifurcation, giving results in excellent agreement with those of direct numerical simulations. A global linear stability analysis will also be used below to investigate the physically similar problem of puffing of a round liquid-pool fire, as is appropriate, given the expected lack of slenderness of the base flow.

In a jet diffusion flame, momentum is injected with the fuel, and consequently the jet Reynolds number plays a role in the flame dynamics, along with the Froude number, those being the two main flow parameters controlling the onset of the flickering instability. In a pool fire, however, the upward motion is induced

* Corresponding author.
E-mail address: wicoenen@ucsd.edu (W. Coenen).

https://doi.org/10.1016/j.combustflame.2018.02.011
0010-2180/© 2018 The Combustion Institute. Published by Elsevier Inc. All rights reserved.

Please cite this article as: D. Moreno-Boza et al., On the critical conditions for pool-fire puffing, Combustion and Flame (2018), https://doi.org/10.1016/j.combustflame.2018.02.011

UNCORRECTED PROOF

by buoyant forces, with negligibly small momentum transfer from the fuel vaporizing from the pool surface. Therefore, apart from the inherent thermochemical parameters, a single dimensionless parameter—the Rayleigh number defined below in Eq. (1)—is seen to characterize the flow. Puffing occurs when the Rayleigh number exceeds a critical value, associated with a critical value of the pool radius.

The objective of the present work is to determine the critical Rayleigh number for pool-fire puffing, using the simplest possible description that still retains the essential physical ingredients. In particular, we employ the limit of infinitely fast chemical reaction, with account taken of the nonunity Lewis number and the vaporization characteristics of typical liquid fuels. It is known that radiation can play an important role in luminous sooting flames, lowering the peak temperature, and increasing the heat transfer to the liquid fuel [5,31,32]. Nevertheless, because it is a volumetric effect, it is expected to be small for the flame sizes associated with the onset of puffing, which, as our analysis will reveal, are on the order of a centimeter. Details of the specific design of the burner, such as the pan lip height, the thermal properties of the pan and its surrounding wall, and the height of the fuel level with respect to the pan rim, can also have a considerable influence on small-scale pool fires [33]. In our analysis, to eliminate the need for solving the complete coupled heat-transfer problem for the solid elements, we purposely focus on two canonical configurations, in which the surrounding horizontal wall is either an adiabatic surface or an isothermal surface at the ambient temperature, and the fuel level is flush with this wall. Our description is aimed to be generally valid for all typical liquid fuels—through an adequate choice of the thermochemical and transport parameters. In this paper, results are presented for methanol and heptane, which are selected as representative of alcohol and hydrocarbon fuels. The values obtained for the critical radius and puffing frequency are compared with those of laboratory experiments, yielding reasonably good agreement, as discussed below.

The paper is structured as follows. In Section 2 a detailed mathematical formulation is given for the description of the dynamics of canonical laminar pool fires. A global stability analysis and its predictions for the critical Rayleigh number are presented in Section 3. Section 4 is devoted to an experimental characterization of the onset of puffing, whereas in Section 5 the associated puffing frequencies are quantified. Finally, concluding remarks are given in Section 6.

2. Mathematical description of laminar pool fires

2.1. Conservation equations

We give below the equations and boundary conditions for the description of the burning of a round pool of liquid fuel with radius a^* in a quiescent air atmosphere with temperature T_A^* and density ρ_A^*. In the presence of buoyancy, fractional density differences of order unity, associated with the temperature increase caused by the chemical heat release, induce velocities of order $v_g^* = g^* a^{*2}/\nu_A^*$ at distances of order a^* from the pool surface. Here g^* is the gravitational acceleration, and ν_A^* is the ambient kinematic viscosity. The Reynolds number based on this velocity is the Grashof number $Gr = g^* a^{*3}/\nu_A^{*2}$, measuring the relative effects of convective acceleration and viscous forces, with the accompanying Rayleigh number

$$Ra = \frac{g^* a^{*3}}{\nu_A^* D_{T,A}^*}, \tag{1}$$

based on the thermal diffusivity of the ambient air $D_{T,A}^*$, being the corresponding Péclet number that measures in the energy-balance equation the ratio of the rates of convective transport and heat conduction. These two parameters, Ra and Gr, related through the Prandtl number $Ra/Gr = Pr = \nu_A^*/D_{T,A}^* \simeq 0.7$, characterize the structure and dynamics of pool fires. In particular, the onset of puffing occurs at a critical value $Ra_c = PrGr_c$, to be determined below.

The pool radius a^* and the characteristic velocity v_g^* will be used as scales for the dimensionless axisymmetric cylindrical coordinates $\boldsymbol{x} = (x, r)$ and velocity $\boldsymbol{v} = (v_x, v_r)$. With the time and the pressure differences from the quiescent ambient hydrodynamic distribution scaled with $t_g^* = a^*/v_g^*$ and $\rho_A^* g^* a^*$ to give the variables t and p, respectively, the continuity and momentum equations become

$$-\frac{1}{\rho}\frac{\mathrm{D}\rho}{\mathrm{D}t} = \boldsymbol{\nabla}\cdot\boldsymbol{v}, \tag{2}$$

$$\frac{Ra}{Pr}\rho\frac{\mathrm{D}\boldsymbol{v}}{\mathrm{D}t} = -\boldsymbol{\nabla}p + (1-\rho)\boldsymbol{e}_x + \boldsymbol{\nabla}\cdot[\mu(\boldsymbol{\nabla}\boldsymbol{v} + \boldsymbol{\nabla}\boldsymbol{v}^T)], \tag{3}$$

where $\mathrm{D}/\mathrm{D}t = \partial/\partial t + \boldsymbol{v}\cdot\boldsymbol{\nabla}$ denotes the substantial derivative and ρ and μ are the density and viscosity scaled with their ambient values. The reaction between the fuel and the oxygen of the air will be considered to occur according to the global irreversible step

$$\mathrm{F} + s\mathrm{O}_2 \rightarrow (1+s)\mathrm{P} + q^*, \tag{4}$$

where s and q^* are the mass of oxygen consumed and the amount of heat released per unit mass of fuel burnt. The associated conservation equations for reactants and energy are

$$Ra\,\rho\frac{\mathrm{D}Y_\mathrm{F}}{\mathrm{D}t} = \frac{1}{Le_\mathrm{F}}\boldsymbol{\nabla}\cdot(\rho D_\mathrm{T}\boldsymbol{\nabla}Y_\mathrm{F}) - w_\mathrm{F}, \tag{5}$$

$$Ra\,\rho\frac{\mathrm{D}Y_\mathrm{O}}{\mathrm{D}t} = \boldsymbol{\nabla}\cdot(\rho D_\mathrm{T}\boldsymbol{\nabla}Y_\mathrm{O}) - Sw_\mathrm{F}, \tag{6}$$

$$Ra\,\rho\frac{\mathrm{D}T}{\mathrm{D}t} = \boldsymbol{\nabla}\cdot\left(\rho D_\mathrm{T}\boldsymbol{\nabla}T\right) + qw_\mathrm{F}, \tag{7}$$

where T is the temperature scaled with T_A^*, and Y_F and $Y_\mathrm{O} = Y_{\mathrm{O}_2}/Y_{\mathrm{O}_{2A}}$ are the mass fraction of fuel vapor and oxygen, the latter normalized with its value $Y_{\mathrm{O}_{2A}} \simeq 0.232$ in air. The dimensionless reaction rate w_F is the mass of fuel consumed by the chemical reaction per unit volume per unit time scaled with ρ_A^*/t_g^*. The thermochemical parameters s and q^* defined above appear in the reaction-rate factors $S = s/Y_{\mathrm{O}_{2A}}$ and $q = q^*/(c_p^* T_A^*)$ in (6) and (7), respectively, where c_p^* denotes the specific heat at constant pressure, assumed to be constant in the following analysis. The parameter S, of order $S = 15$ in hydrocarbon combustion, represents the amount of air needed to burn the unit mass of fuel. The other parameter, q, is the heat release per unit mass of fuel scaled with the ambient enthalpy, which takes fairly large values for typical fuels, such that $q/S \sim 7$.

The presence of soot is noticeable in most liquid-pool flames, enhancing heat losses through radiation. Since this effect is anticipated to be moderately small for the small-size flames associated with the onset of puffing, no radiation term is included in (7). Instead, its effect on the peak flame temperature will be approximately accounted for by slightly lowering the value of the dimensionless heat release q.

Similar to the other transport properties, the thermal diffusivity D_T appearing in (5)–(7) is scaled with its ambient air value $D_{T,A}^*$. The presumed power laws

$$\mu = \rho D_\mathrm{T} = T^\sigma \tag{8}$$

will be used below for the temperature variation of the transport properties, with $\sigma = 0.7$ employed in the numerical integrations. A Fickian model is used for the diffusion velocities of the reactants, a sufficiently accurate approximation in fuel-air combustion,

UNCORRECTED PROOF

Please cite this article as: D. Moreno-Boza et al., On the critical conditions for pool-fire puffing, Combustion and Flame (2018), https://doi.org/10.1016/j.combustflame.2018.02.011

where the dominant presence of nitrogen molecules simplifies the description of molecular transport, and fuel molecules typically are not large enough for Soret transport to become important. While a unity Lewis number has been employed for oxygen, an excellent approximation under most conditions, a non-unity Lewis number $Le_F > 1$ is used for the fuel, as is needed for accuracy in computations of most hydrocarbon and alcohol fuels.

The motion induced is very slow and involves small spatial pressure variations that can be neglected in an excellent approximation when writing the equation of state,

$$\rho T = \left[Y_F \left(\frac{W_A^*}{W_F^*} - 1 \right) + 1 \right]^{-1}. \tag{9}$$

The molecular mass of most liquid fuels W_F^* is significantly larger than that of the air W_A^*, so that the density differences induced by the presence of the fuel vapor have been included in (9), while neglecting the departures from W_A^* of the molecular mass of all other species, a sufficiently accurate approximation under most conditions.

In specifying the boundary condition for the velocity in the air atmosphere, account must be taken of the presence of a buoyant plume near the axis as well as the surrounding flow induced by the plume entrainment. Alternatively, to facilitate the numerical integration, a stress-free condition can be used at the boundary of the computational domain. The resulting boundary conditions, including the temperature and composition of the surrounding air atmosphere, become

$$-p\boldsymbol{n} + \boldsymbol{n} \cdot \left[\mu (\boldsymbol{\nabla v} + \boldsymbol{\nabla v}^T) \right] = T - 1 = Y_F = Y_O - 1 = 0 \tag{10}$$

as $x^2 + r^2 \gg 1$ for $x \neq 0$, where $\boldsymbol{n}$ denotes the unit vector normal to the far-field surface bounding the computational domain.

The surface $r > 1$, $x = 0$ of the wall that surrounds the fuel pool is assumed to be impermeable and chemically inert, thereby providing the additional boundary conditions

$$v_x = v_r = \frac{\partial Y_F}{\partial x} = \frac{\partial Y_O}{\partial x} = 0. \tag{11}$$

The thermal properties of this surface can have a significant influence on the flame, with realistic cases falling in between the extreme limits corresponding to either an adiabatic surface,

$$\frac{\partial T}{\partial x} = 0, \tag{12}$$

or an isothermal surface at the ambient temperature,

$$T = 1. \tag{13}$$

Fuel vaporization occurs with a prescribed dimensionless boiling temperature T_B and dimensionless latent heat of vaporization $L_v = L_v^*/(c_p^* T_A^*)$. The energy invested in raising the temperature of the liquid fuel, with specific heat c_l^*, from the ambient to the boiling temperature is taken into account by defining an effective heat of vaporization $l_v = L_v + (T_B - 1)c_l^*/c_p^*$. The resulting boundary conditions on the vaporizing fuel surface (i.e. at $x = 0$ for $r < 1$) become

$$v_r = T - T_B = 0 \tag{14}$$

$$Ra\, \rho v_x Y_F - \frac{T_B^\sigma}{Le_F} \frac{\partial Y_F}{\partial x} = Ra\, \rho v_x \tag{15}$$

$$Ra\, \rho v_x Y_O - T_B^\sigma \frac{\partial Y_O}{\partial x} = 0 \tag{16}$$

$$Ra\, \rho v_x T - T_B^\sigma \frac{\partial T}{\partial x} = -l_v Ra\, \rho v_x \tag{17}$$

when written in dimensionless form.

2.2. Coupling functions for nonpremixed combustion with $Le_F \neq 1$

Our analysis employs the fast-reaction limit in which the chemical-reaction terms in (5)–(7) appear as Dirac delta distributions along a flame surface separating an outer ambient region with no fuel vapor from an inner region surrounding the pool surface with no oxygen, so that the equilibrium condition

$$Y_F Y_O = 0 \tag{18}$$

applies. To facilitate the analysis of the fast-reaction limit it is convenient to describe the flow in terms of chemistry-free coupling functions, with associated conservation equations obtained by eliminating the reaction terms through appropriate linear combinations of (5)–(7) [34]. The specific selection of coupling functions for the present study is that employed earlier [35] for the analysis of counterflow gaseous diffusion flames. The derivation begins by multiplying (6) by q/S and adding (7) to provide a chemistry-free conservation equation for the coupling function $(T + qY_O/S)$, which can be conveniently expressed as a normalized excess enthalpy

$$\xi = \frac{T - 1 + (q/S)(Y_O - 1)}{T_B - 1 - q/S}, \tag{19}$$

whose transport equation is

$$Ra\, \rho \frac{D\xi}{Dt} = \boldsymbol{\nabla} \cdot \left(\rho D_T \boldsymbol{\nabla} \xi \right). \tag{20}$$

With the normalization employed in (19), the excess enthalpy ξ is zero in the air atmosphere and unity on the fuel surface.

The reaction term can also be eliminated by subtracting (6) from (5) times S. When the Lewis number L_F is different from unity, the resulting transport equation exhibits a coupling function $(SY_F - Y_O)$ in the accumulation and convective terms that is different from the coupling function $(SY_F/Le_F - Y_O)$ appearing in the diffusion term. When these coupling functions are normalized, we obtain a diffusion-weighted mixture fraction

$$\tilde{Z} = \frac{SY_F/Le_F - Y_O + 1}{S/Le_F + 1}, \tag{21}$$

arising from the diffusion term, in addition to the classical mixture fraction

$$Z = \frac{SY_F - Y_O + 1}{S + 1}, \tag{22}$$

resulting in the conservation equation

$$Ra\, \rho \frac{DZ}{Dt} = \frac{1}{Le} \boldsymbol{\nabla} \cdot (\rho D_T \boldsymbol{\nabla} \tilde{Z}), \tag{23}$$

where $Le = (S + 1)/(S/Le_F + 1)$.

To solve (20) and (23) coupled with (2) and (3) and supplemented with (8) and (9), we need to relate T, Y_F, and Z to ξ and $\tilde{Z}$. These relations can be obtained by using the fast-reaction condition (18) of non-coexistence of Y_O and Y_F, which are simultaneously zero at the flame, given by the isosurface $Z = Z_S = 1/(1 + S)$, or $\tilde{Z} = \tilde{Z}_S = 1/(1 + S/Le_F)$, as follows from the definitions (21) and (22). For $\tilde{Z} \geq \tilde{Z}_S$

$$Y_O = 0, \tag{24}$$

$$Y_F = \frac{Z - Z_S}{1 - Z_S} = \frac{\tilde{Z} - \tilde{Z}_S}{1 - \tilde{Z}_S}, \tag{25}$$

$$T - 1 = \left(T_B - 1 - \frac{q}{S} \right) \xi + \frac{q}{S}, \tag{26}$$

whereas for $\tilde{Z} \leq \tilde{Z}_S$

$$Y_F = 0, \tag{27}$$

UNCORRECTED PROOF

Please cite this article as: D. Moreno-Boza et al., On the critical conditions for pool-fire puffing, Combustion and Flame (2018), https://doi.org/10.1016/j.combustflame.2018.02.011

$$1 - Y_O = \frac{Z}{Z_S} = \frac{\tilde{Z}}{\tilde{Z}_S}, \tag{28}$$

$$T - 1 = \left(T_B - 1 - \frac{q}{S}\right)\xi + \frac{q}{S}\frac{\tilde{Z}}{\tilde{Z}_S}. \tag{29}$$

Eqs. (24)–(29) provide piecewise linear relations for the evaluation of Y_F, Y_O, and Z in terms of $\tilde{Z}$. In addition, the last relation in the equations gives T in terms of $\tilde{Z}$ and ξ.

The boundary conditions (10)–(17) become

$$-p\boldsymbol{n} + \boldsymbol{n}\cdot\left[\mu(\nabla\boldsymbol{v} + \nabla\boldsymbol{v}^T)\right] = \xi = \tilde{Z} = 0 \tag{30}$$

as $(x^2 + r^2) \to \infty$ for $x \neq 0$, together with

$$v_x = v_r = \frac{\partial\tilde{Z}}{\partial x} = 0, \quad \text{at } x = 0 \text{ for } r > 1, \tag{31}$$

and

$$\left.\begin{aligned} v_r &= \xi - 1 = 0, \\ -T_B^{\sigma}\frac{\partial\xi}{\partial x} &= \alpha Ra\,\rho v_x \\ -T_B^{\sigma}\frac{\partial\tilde{Z}}{\partial x} &= Le_F Ra\,\rho v_x(1-\tilde{Z}) \end{aligned}\right\} \text{ at } x = 0 \text{ for } r < 1, \tag{32}$$

where

$$\alpha = \frac{l_v + T_B}{q/S + 1 - T_B}. \tag{33}$$

The definition of the problem is completed by specifying the thermal boundary condition at the surrounding wall, $x = 0$, $r > 1$, which, for the case of an adiabatic surface may be written as

$$\frac{\partial\xi}{\partial x} = 0, \tag{34}$$

whereas the conditions become

$$\xi = \begin{cases} \dfrac{q/S}{q/S + 1 - T_B} & \text{for } \tilde{Z} \geq \tilde{Z}_S, \\ \dfrac{q/S}{q/S + 1 - T_B}\dfrac{\tilde{Z}}{\tilde{Z}_S} & \text{for } \tilde{Z} \leq \tilde{Z}_S. \end{cases} \tag{35}$$

for the case of an isothermal surrounding wall at ambient temperature, as follows from (26) and (29).

2.3. Representative thermochemical and transport parameters for methanol and heptane pool flames

The formulation presented previously is generally valid for any fuel, given an adequate choice of thermochemical parameters. In the present work, specific attention is directed to methanol and to heptane, whose molecular weights are such that $W_F^*/W_A^* = 1.1$ and $W_F^*/W_A^* = 3.45$, respectively. Also, with ambient air assumed to be at $T_A^* = 300$ K, their respective dimensionless boiling temperatures T_B and effective heat of vaporization l_v are $T_B = 1.12$ and $l_v = 2.84$ for methanol and $T_B = 1.24$ and $l_v = 1.14$ for heptane.

According to the stoichiometry of the overall oxidation reaction $2CH_3OH + 3O_2 \to 2CO_2 + 4H_2O$, the oxygen-to-fuel ratio for methanol–air combustion is $s = 1.5 \times 32/W_F^* = 1.50$, so that $S = s/0.232 = 6.47$. On the other hand, the amount of heat released per unit mass of fuel consumed is $q^* = (h^o_{CO_2} + 2h^o_{H_2O} - h^o_{CH_3OH})/W_F^* \simeq 21$ kJ/g, where h_i^o is the molar enthalpy of formation of species i. The associated dimensionless heat of reaction can be evaluated for $T_A^* = 300$ K with a presumed value of $c_p^* = 1400$ J/(kg K) to give $q = q^*/(c_p^* T_A^*) \simeq 50$, thereby yielding $q/S = 50/6.47 \simeq 7.7$ in (26), (29), (33), and (35).

Analogously, for heptane the overall oxidation reaction $C_7H_{16} + 11O_2 \to 7CO_2 + 8H_2O$ gives $s = 11 \times 32/W_F^* = 3.52$, so that $S = s/0.232 = 15.2$. The amount of heat released per unit mass of fuel consumed is $q^* = (7h^o_{CO_2} + 8h^o_{H_2O} - h^o_{C_7H_{16}})/W_F^* \simeq 45$ kJ/g, with associated dimensionless heat of reaction $q = q^*/(c_p^* T_A^*) \simeq 107$, resulting in $q/S = 107/15.2 \simeq 7$. As previously mentioned, since heptane is a sooting fuel, this value is to be lowered in the model as an approximate way to account for the heat losses due to radiation. In particular, the value $q/S = 5.5$ is to be used for the following integrations, resulting in a peak flame temperature on the order of 1750 K.

The selection of the Lewis number of the fuel must account for the fact that its value can vary considerably with the local mixture composition, mainly as a result of the large specific heat of heavy hydrocarbon molecules. For instance, in heptane flames the expected values of Le_F range from about $Le_F = 1.1$ at the vaporizing fuel surface, where the fuel content is significant, thereby lowering noticeably the local thermal diffusivity, to $Le_F = 2.6$ at the flame sheet, where the mixture is composed of nitrogen and combustion products. To reflect this variation in our constant-Lewis-number formulation, a conveniently selected intermediate value $Le_F = 1.8$ is employed in the numerical results shown below. For methanol on the other hand, this variation is much less pronounced (i.e. $1.10 \lesssim Le_F \lesssim 1.2$); the value $Le_F = 1.15$ is to be employed in the numerical computations.

3. Puffing as a hydrodynamic global mode

Recent analyses have shown that the flickering of low-density jets [36], jet diffusion flames [30], and buoyant plumes [37,38] is a manifestation of a hydrodynamic global instability, the onset of which can be computed with a linear global stability analysis. The same type of global instability is anticipated to be responsible for the puffing of liquid-pool fires. The application of the linear stability formalism to this problem involves introduction of a normal-mode decomposition of the form

$$(\boldsymbol{v}, p, \tilde{Z}, \xi) = (\bar{\boldsymbol{v}}, \bar{p}, \bar{\tilde{Z}}, \bar{\xi})(\boldsymbol{x}) + \epsilon(\hat{\boldsymbol{v}}, \hat{p}, \hat{\tilde{Z}}, \hat{\xi})(\boldsymbol{x})e^{-i\omega t} \tag{36}$$

with $\epsilon \ll 1$ being an infinitesimally small perturbation parameter. The solution begins with the determination of the steady base flow $(\bar{\boldsymbol{v}}, \bar{p}, \bar{\tilde{Z}}, \bar{\xi})(\boldsymbol{x})$. Linearizing then the conservation equations about this base solution provides a set of linear conservation equations for the complex eigenfunctions $(\hat{\boldsymbol{v}}, \hat{p}, \hat{\tilde{Z}}, \hat{\xi})(\boldsymbol{x})$, which satisfy homogeneous boundary conditions. The resulting generalized eigenvalue problem determines the complex eigenvalues $\omega = \omega_r + i\,\omega_i$, whose real part ω_r determines the frequency of the perturbation, while the imaginary part ω_i represents its growth rate, thereby determining whether the flow is globally unstable ($\omega_i > 0$) or globally stable ($\omega_i < 0$).

3.1. Computations of steady liquid-pool flames

The base flow corresponding to a given Rayleigh number is obtained by numerical integration of the steady form of the governing equations (2), (3), (20) and (23), supplemented with the relations (8), (9), (24)–(29), and subject to the boundary conditions (30)–(35). To avoid potential instability issues in the calculation of the base flow for large Rayleigh numbers, the numerical integration employs a root-finding scheme according to the following fixed-point iteration procedure. Given an initial guess for the coupling functions ξ and $\tilde{Z}$, the mixture fraction Z, temperature T, density ρ, and transport properties are computed with use made of (8), (9), and (24)–(29). This information is then supplied to Eqs. (2) and (3), allowing us to compute the velocity and pressure fields by means of a Newton–Raphson algorithm. The velocity is used to evaluate the convective derivatives in (20) and (23),

UNCORRECTED PROOF

Please cite this article as: D. Moreno-Boza et al., On the critical conditions for pool-fire puffing, Combustion and Flame (2018), https://doi.org/10.1016/j.combustflame.2018.02.011

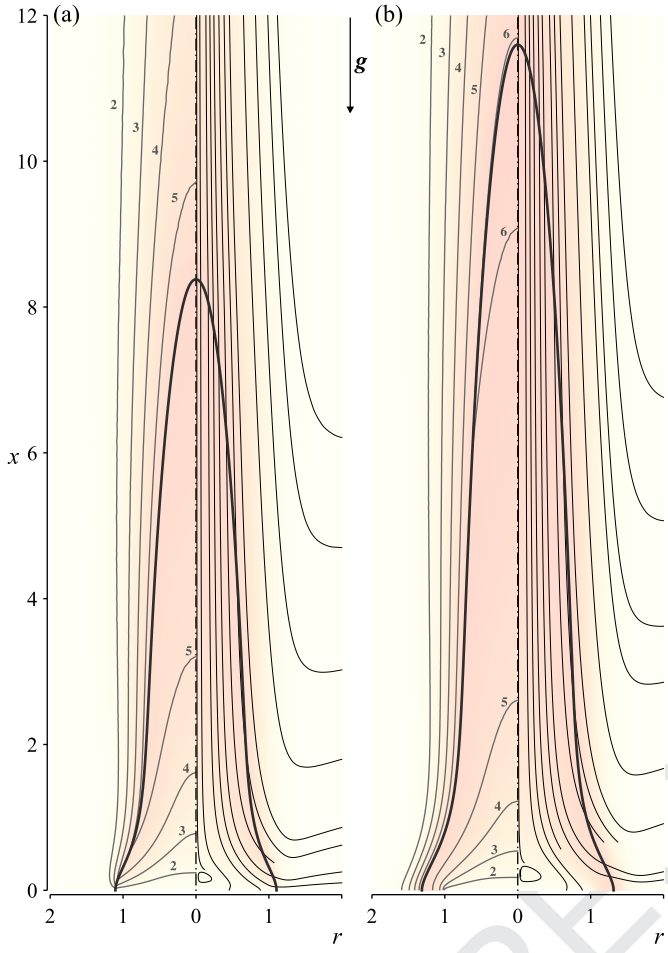

Fig. 1. Steady solutions for a heptane pool fire at $Ra = 10{,}000$ with (a) isothermal, and (b) adiabatic boundary conditions on the surrounding surface. The left part of each plot shows equispaced isotherms along with their corresponding temperature values; sample streamlines are shown on the right-hand sides. The solid line indicates the stoichiometric line $\tilde{Z} = \tilde{Z}_S$.

yielding new values for the coupling functions. The process is repeated until relative changes of $\tilde{Z}$ and ξ in subsequent iterations are less than a prescribed tolerance of 10^{-6}.

The discretization of the problem is performed with the software FreeFem++ using Taylor-Hood elements ($P2$ for velocity and coupling functions and $P1$ for the pressure field to satisfy the Ladyzhenskaja–Babuška–Brezzi condition). Details of the discretization method, used for instance by [39], can be found in [40]. The grid is adapted to the solution using a Delaunay triangulation of the computational domain $\boldsymbol{x} \in [0,\, x_{\max}] \times [0,\, r_{\max}]$. The size of the computational box and the grid refinement level are varied until convergence is achieved, with typical values $(x_{\max}, r_{\max}) = (150, 50)$ used in the numerical integrations reported below.

Illustrative sample results of integrations are shown in Fig. 1. The two plots show the structure of a steady heptane flame at $Ra = 10{,}000$ for the cases of an isothermal wall (a) and an adiabatic wall (b), including isotherms (left-hand side of each plot) and accompanying streamlines (right-hand side of each plot). It can be seen how air is entrained radially towards the flame zone, and how the combustion products are advected upward by the action of buoyancy. With an adiabatic wall, the flame is seen to extend noticeably farther outside the edge of the pool at its base. In the far field (not shown), the flame can be considered as a point source of heat, and consequently the flow field becomes that of a thermal plume [41].

It is known that the buoyant acceleration of the flow in the central region of the flame causes the radial profiles of axial velocity to exhibit inflection points along the flame envelope, a region characterized by low values of the advection velocity [30,42,43]. From a local stability point of view, this scenario allows for the possibility of an absolutely unstable flow. The destabilization of the flow is further enhanced by buoyant vorticity production in the flame envelope, whose presence is clearly implied in Fig. 1a and b by the strong radial temperature (and thus density) gradients. The comparison between the two cases shown in Fig. 1 reveals that heat loss to the isothermal wall at temperature $T = 1$ causes the flame to be considerably shorter than that of the adiabatic case. The shorter size results in lower buoyancy-induced velocities and larger viscous stresses and heat-loss rates. Furthermore, the flame temperature, varying along the flame, is approximately 10% lower in the isothermal case, reducing the density gradients and therefore the buoyant vorticity production. All these effects have a stabilizing influence and should result in larger values of the critical Rayleigh number for flames bounded by isothermal walls, compared to the adiabatic counterpart. The results of the global stability analysis, which will be presented in Section 3.3, confirm this logic.

3.2. The generalized eigenvalue problem

Introduction of the normal-mode decomposition (36) in the governing equations and linearization around the base state described in Section 3.1 produces the linearized equations

$$-\mathrm{i}\omega\,\hat{\rho} + \boldsymbol{\nabla}\cdot\hat{\rho}\bar{\boldsymbol{v}} + \boldsymbol{\nabla}\cdot\bar{\rho}\hat{\boldsymbol{v}} = 0, \tag{37}$$

$$\begin{aligned}\tfrac{Ra}{Pr}\big(-\mathrm{i}\omega\bar{\rho}\,\hat{\boldsymbol{v}} + \hat{\rho}\bar{\boldsymbol{v}}\cdot\boldsymbol{\nabla}\bar{\boldsymbol{v}} + \bar{\rho}\hat{\boldsymbol{v}}\cdot\boldsymbol{\nabla}\bar{\boldsymbol{v}} + \bar{\rho}\bar{\boldsymbol{v}}\cdot\boldsymbol{\nabla}\hat{\boldsymbol{v}}\big) &= -\boldsymbol{\nabla}\hat{p}\\ -\hat{\rho}\boldsymbol{e}_x + \boldsymbol{\nabla}\cdot\big[\hat{\mu}(\boldsymbol{\nabla}\bar{\boldsymbol{v}} + \boldsymbol{\nabla}\bar{\boldsymbol{v}}^{\mathrm{T}}) + \bar{\mu}\big(\boldsymbol{\nabla}\hat{\boldsymbol{v}} + \boldsymbol{\nabla}\hat{\boldsymbol{v}}^{\mathrm{T}}\big)\big],\end{aligned} \tag{38}$$

$$\begin{aligned}-\mathrm{i}\omega\bar{\rho}\,\hat{\tilde{Z}} + \hat{\rho}\bar{\boldsymbol{v}}\cdot\boldsymbol{\nabla}\bar{\tilde{Z}} + \bar{\rho}\hat{\boldsymbol{v}}\cdot\boldsymbol{\nabla}\bar{\tilde{Z}} + \bar{\rho}\bar{\boldsymbol{v}}\cdot\boldsymbol{\nabla}\hat{\tilde{Z}}\\ = \tfrac{1}{Le\,Ra}\boldsymbol{\nabla}\cdot\Big(\hat{\mu}\boldsymbol{\nabla}\bar{\tilde{Z}} + \bar{\mu}\boldsymbol{\nabla}\hat{\tilde{Z}}\Big),\end{aligned} \tag{39}$$

$$\begin{aligned}-\mathrm{i}\omega\bar{\rho}\,\hat{\xi} + \hat{\rho}\bar{\boldsymbol{v}}\cdot\boldsymbol{\nabla}\bar{\xi} + \bar{\rho}\hat{\boldsymbol{v}}\cdot\boldsymbol{\nabla}\bar{\xi} + \bar{\rho}\bar{\boldsymbol{v}}\cdot\boldsymbol{\nabla}\hat{\xi}\\ = \tfrac{1}{Ra}\boldsymbol{\nabla}\cdot\Big(\hat{\mu}\boldsymbol{\nabla}\bar{\xi} + \bar{\mu}\boldsymbol{\nabla}\hat{\xi}\Big),\end{aligned} \tag{40}$$

for the eigenfunctions $(\hat{\boldsymbol{v}}, \hat{p}, \hat{\tilde{Z}}, \hat{\xi})(\boldsymbol{x})$, where

$$\hat{\mu} = \sigma\bar{T}^{\sigma-1}\hat{T}, \tag{41}$$

$$\hat{T} = (\partial T/\partial\xi)\,\hat{\xi} + (\partial T/\partial\tilde{Z})\,\hat{\tilde{Z}}, \tag{42}$$

$$\hat{\rho} = (\partial\rho/\partial\xi)\,\hat{\xi} + (\partial\rho/\partial\tilde{Z})\,\hat{\tilde{Z}}, \tag{43}$$

$$\hat{Z} = (\partial Z/\partial\tilde{Z})\,\hat{\tilde{Z}}, \tag{44}$$

represent the perturbed viscosity, temperature, density and mixture fraction, respectively, conveniently expressed with use made of the chain rule. The derivatives appearing in (42)–(44), to be determined from (9), (25), (26), (28), and (29), must be evaluated with the local values of $\bar{\tilde{Z}}$ and $\bar{\xi}$. The linear system (37)–(40) is to be integrated with the boundary conditions

$$\hat{\boldsymbol{v}} = \frac{\partial\hat{\tilde{Z}}}{\partial x} = \hat{T} = 0 \tag{45}$$

at the wall,

$$-\hat{p}\boldsymbol{n} + \boldsymbol{n}\cdot\big[\hat{\mu}\big(\boldsymbol{\nabla}\bar{\boldsymbol{v}} + \boldsymbol{\nabla}\bar{\boldsymbol{v}}^{\mathrm{T}}\big) + \bar{\mu}\big(\boldsymbol{\nabla}\hat{\boldsymbol{v}} + \boldsymbol{\nabla}\hat{\boldsymbol{v}}^{\mathrm{T}}\big)\big] = 0, \tag{46}$$

UNCORRECTED PROOF

$$\hat{\tilde{Z}} = \hat{\xi} = 0 \tag{47}$$

at the lateral and outflow boundaries, and

$$\hat{v}_r = 0, \tag{48}$$

$$\frac{T_B^\sigma}{\alpha Ra}\frac{\partial \hat{\xi}}{\partial x} + \hat{\rho}\bar{v}_x + \bar{\rho}\hat{v}_x = 0, \tag{49}$$

$$\frac{T_B^\sigma}{Le_F Ra}\frac{\partial \hat{\tilde{Z}}}{\partial x} + \left(\hat{\rho}\bar{v}_x + \bar{\rho}\hat{v}_x\right)(1-\tilde{\bar{Z}}) - \bar{\rho}\bar{v}_x\hat{\tilde{Z}} = 0, \tag{50}$$

$$\hat{\xi} = 0 \tag{51}$$

at the vaporizing fuel boundary.

Nontrivial solutions to the generalized eigenvalue problem defined in (37)–(51) exist for a discrete set of complex values of $\omega = \omega_r + i\,\omega_i$. As previously mentioned, the imaginary part of ω represents the growth rate of the perturbation, so that its sign determines whether the flow is globally unstable ($\omega_i > 0$) or globally stable ($\omega_i < 0$), whereas its real part ω_r provides the frequency of the perturbation, with corresponding Strouhal number $St = \omega_r/\pi$ (based on the diameter, to follow the convention most commonly used in the literature).

3.3. Stability predictions for methanol and heptane flames

The finite-element formalism described earlier for the steady solution was also employed to discretize the perturbed equations, but using instead a split mesh with twice the number of nodes that was used for the base flow. The eigenvalue problem was solved by a shift-inverse power method [44], providing the eigenvalues ω and associated eigenfunctions $(\hat{v}, \hat{p}, \hat{\tilde{Z}}, \hat{\xi})(\boldsymbol{x})$.

Figure 2 shows the resulting eigenvalue spectra for the four canonical cases under consideration here, i.e. methanol and heptane fuel pools, surrounded by either an adiabatic or an isothermal wall, for respective values of the Rayleigh number such that the flow is marginally stable. This means (except for one of the four cases, to be discussed in detail below) that all eigenvalues lie in the stable lower half plane, the most unstable mode having a zero growth rate. Any increase in the Rayleigh number would cause the latter mode to achieve a positive growth rate, and the flow to undergo a Hopf bifurcation to a globally unstable state.

For methanol pool flames (Fig. 2a), the spectra share characteristics with those encountered recently in diffusion flames [30] and low-density jets [36], in that the leading eigenvalue lies isolated from the rest of the spectrum, and it is very robust with respect to changes in the numerical implementation, in particular to the axial extent of the computational domain and the mesh refinement—in contrast to the rest of the spectrum. The frequency (Strouhal number) of the leading eigenvalue has approximately the same value $St \simeq 0.0034$ for the marginally stable flames with adiabatic and isothermal walls. The eigenfunctions of axial velocity and temperature accompanying the dominant eigenmode for the isothermal case are shown in Fig. 3. Although the flame is relatively slender, the wavelength of the eigenmodes is seen to be comparable to the flame height, thereby underscoring the need for a biglobal analysis, that is, a global analysis having two-dimensional eigenfunctions (rather than a local quasi-parallel analysis involving only one-dimensional eigenfunctions) to deal with the nonparallel character of the instability.

For heptane flames (Fig. 2b) with an isothermal boundary condition at the wall in contact with the flame, apart from the dominant, well-converged, eigenmode with frequency $St \simeq 0.0035$,

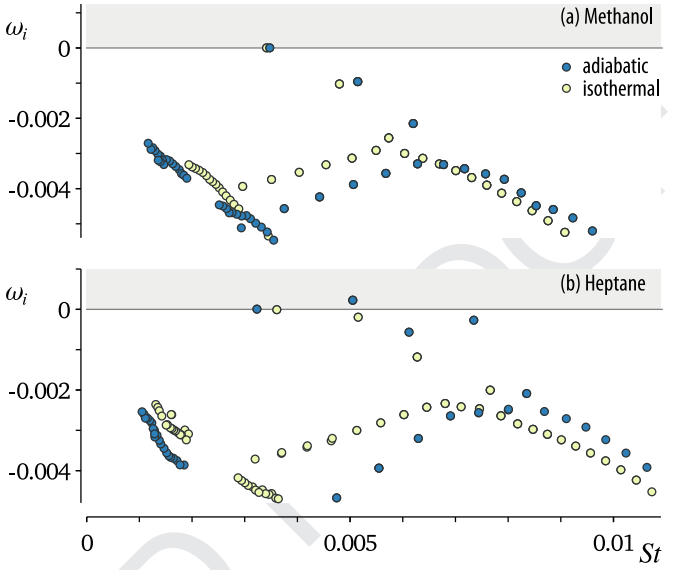

Fig. 2. Global eigenvalue spectra at the verge of global instability for (a) methanol with an adiabatic ($Ra = 19{,}400$, dark blue) or an isothermal ($Ra = 25{,}000$, light yellow) surrounding surface, and (b) heptane with an adiabatic ($Ra = 17{,}800$, dark blue) or an isothermal ($Ra = 18{,}200$, light yellow) surrounding surface. (For interpretation of the references to color in this figure legend, the reader is referred to the web version of this article.)

a second mode is seen to gain importance, with a higher frequency, $St \simeq 0.005$, and with a growth rate that is only slightly negative. Although the frequency of the latter eigenvalue was found to be robust, its growth rate shows some dependence on the domain length. When the boundary condition on the surrounding wall is changed to that of an adiabatic wall, the formerly leading low-frequency eigenvalue loses its dominance to the second, higher-frequency mode. Again, the frequency of the latter was found to be robust, whereas its growth rate was not. Domain-sensitive modes have also been encountered recently for low-density jets at high Reynolds numbers [36], appearing in the form of a so-called arc branch of modes, equally spaced in frequency. The existence of the arc branch was linked to spurious feedback from the outflow boundary on the basis of (i) the branch being aligned with an isocontour of the pseudospectrum, and (ii) the associated eigenfunctions exhibiting an integer number of instability wavelengths between the domain inflow and outflow boundaries. In the buoyant heptane pool flame under consideration here, the domain-sensitive modes have neither of these two characteristics (not shown here), which eliminates such a feedback mechanism as their cause.

For methanol flames, and also for heptane flames surrounded by an isothermal wall, the results of the global stability analysis establish unambiguously the value of the critical Rayleigh number Ra_c for the onset of puffing as the value of Ra at which the growth rate ω_i of the dominant eigenvalue vanishes. The resulting values of Ra_c are summarized as the first in each triplet of entries in Fig. 4; the other two members of the triplet are associated with analysis of the experimental observations, to be discussed in a later section, and they are to be ignored here. For heptane flames surrounded by an adiabatic wall the existence of a high–frequency mode with an ill-defined growth rate (in addition to the robust lower-frequency mode of slightly smaller growth rate) complicates the determination of the critical Rayleigh number; computations for various axial-domain extents revealed that, depending on the eigenvalue selected, the predictions of Ra_c may differ by as much as 15%. Because of the variability of the results associated with the higher-frequency mode, we choose to include in Fig. 4 the value

UNCORRECTED PROOF

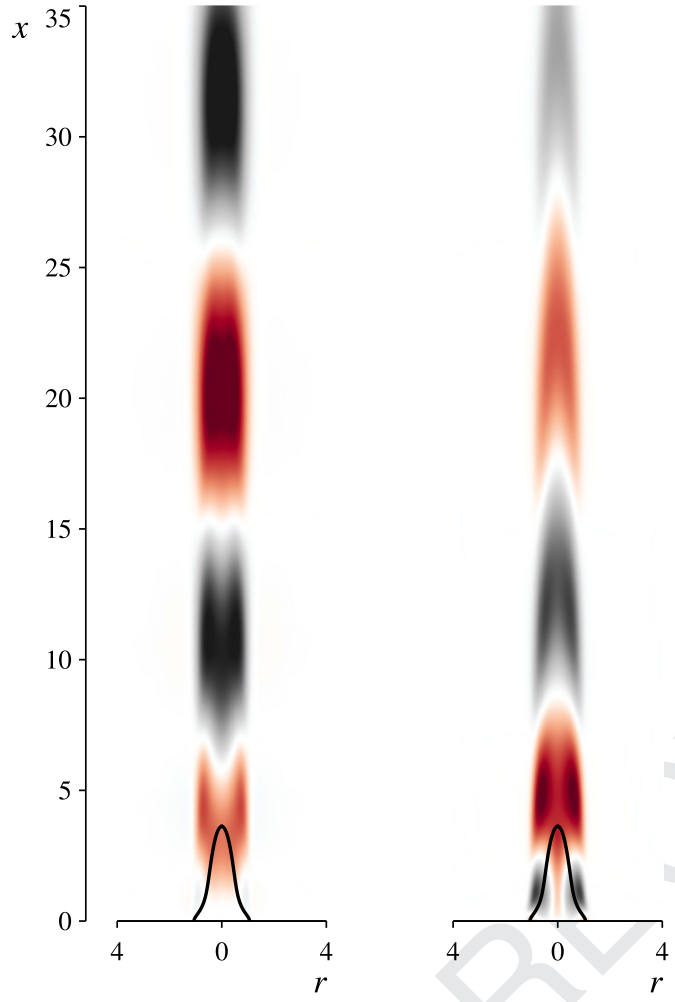

Fig. 3. (Normalized) eigenfunctions for (left) the axial velocity $\hat{v}_x$ and (right) the mixture fraction $\hat{Z}$ associated with the leading eigenvalue for a methanol flame surrounded by an isothermal wall at the onset of instability, $Ra = Ra_c = 25{,}000$ (spectrum represented in Fig. 2a).The thick black line indicates the stoichiometric surface of the corresponding steady base flame.

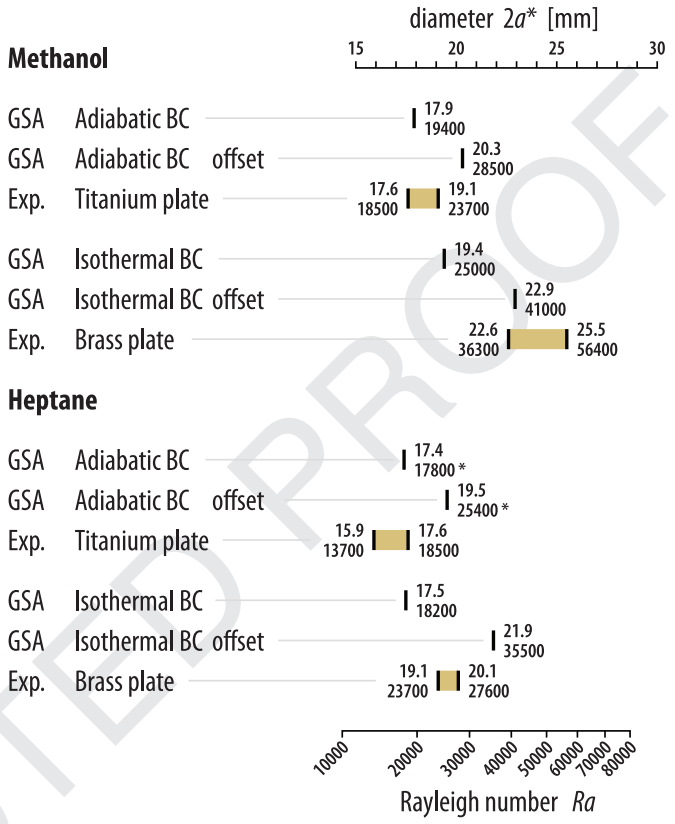

Fig. 4. Critical Rayleigh numbers and corresponding diameters obtained from a global stability analysis (GSA), and from experiments (Exp).

of Ra_c corresponding to the lower-frequency mode, which results in a robust prediction independent of the spatial domain used in the computation. An observation than can be made from this figure is that for both methanol and heptane, when the surface surrounding the fuel pool is adiabatic instead of isothermal, the resulting flame is more unstable, exhibiting a lower associated critical Rayleigh number.

According to the Rayleigh number definition (1), the results for Ra_c translate into predictions of critical diameters $2a_c^*$ according to $a_c^* = (Ra_c \nu_A^* D_{T,A}^* / g^*)^{1/3}$. Using $g^* = 9.807\,\mathrm{m/s^2}$, $\nu_A^* = 1.597 \times 10^{-5}\,\mathrm{m^2/s}$, and $D_{T,A}^* = 2.256 \times 10^{-5}\mathrm{m^2/s}$ in the evaluations yields the values of the critical diameters listed in Fig. 4. Similarly, the pulsating frequency f^* is related to the critical Strouhal number by $f^* = St_c\, g^* a_c^* / (2\nu_A^*)$, yielding values on the order of $f^* \simeq 10\,\mathrm{Hz}$; puffing frequencies and comparisons with experiments will be discussed later.

It is worth mentioning here that the magnitude of the nondimensional numbers $Ra_c \gg 1$ and $St_c \ll 1$ arising from the analysis is a result of the selection of scales for the nondimensional formulation, based on the properties of the cold ambient air (as was needed for the parametric investigations considered). Thus, because of their large temperature dependence $\nu \sim D_T \propto T^{\sigma+1}$, the kinematic viscosity and the thermal diffusivity near the flame are larger than the ambient values ν_A^* and $D_{T,A}^*$ used in the definition of the Rayleigh number (1) by a factor of about 25. As a result, if based on the flame properties, the resulting critical Rayleigh number would be considerably smaller, on the order of a few tens. Likewise, if the characteristic time $\nu_A^*/(g^* a^*)$ had been based instead on the flame value of the kinematic viscosity, the resulting value of St_c would be about 0.1.

4. Experiments

4.1. Experimental setup

To test predictions, controlled experiments were carried out for round pool flames of methanol and heptane with radii in the vicinity of the predicted critical value, so as to observe near-bifurcation states. The experimental setup, depicted in Fig. 5, consists of a 90 cm × 90 cm × 12.7 mm PVC table that holds in its center a removable liquid fuel burner. This burner is composed of a 20 cm × 20 cm × 6.35 mm aluminum plate, a 6 cm-diameter conical polypropylene fuel holder mounted underneath, and a small interchangeable 7.5 cm × 7.5 cm × 3.175 mm plate placed within a recess in the upper side of the former. This interchangeable plate has a circular hole of radius a^* in its center, filled nearly to the rim with a layer of glass beads (0.5 mm in diameter) that rests on a thin stainless steel mesh. This porous layer prevents convective currents in the fuel from affecting the observations. To address the influence of the thermal properties of the surface in contact with the flame, experiments were carried out using two different materials for the interchangeable plate, namely brass and titanium. The thermal conductivities of these metals ($k_{\mathrm{brass}} \simeq 120\,\mathrm{W/(m\,K)}$ and $k_{\mathrm{titanium}} \simeq 15\,\mathrm{W/(m\,K)}$) differ by a factor of approximately 8, the former closer to isothermal conditions and the latter more nearly adiabatic. When assembled, the aluminum plate, the

UNCORRECTED PROOF

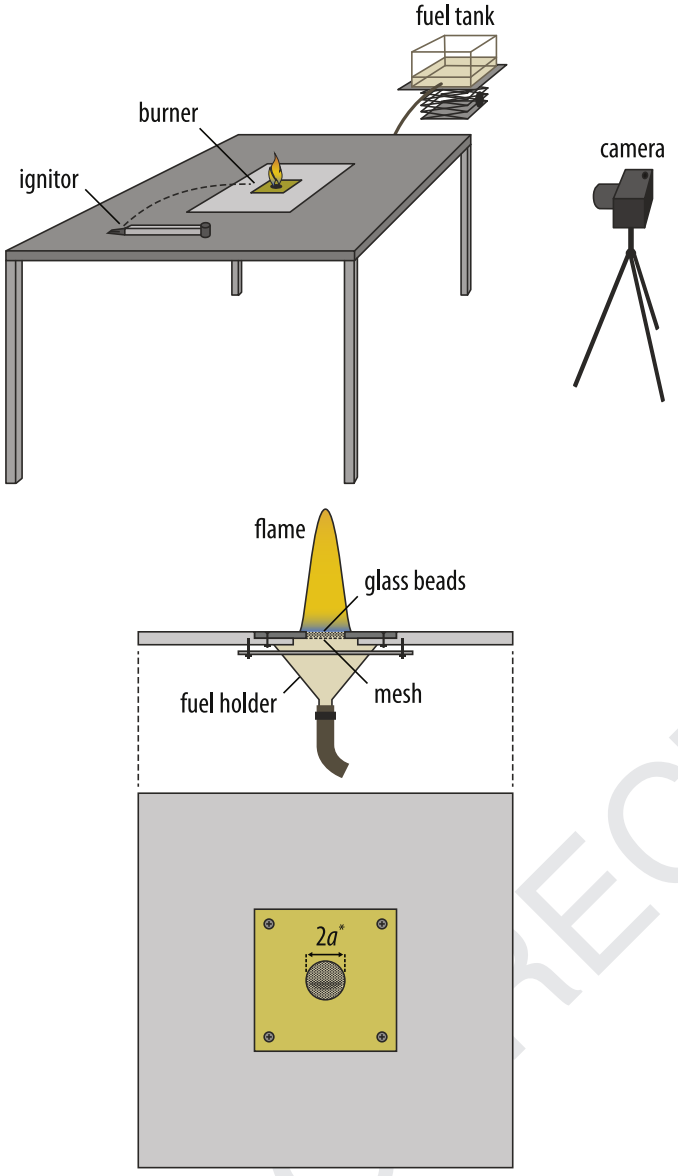

Fig. 5. Schematic view of the experimental setup. The upper diagram shows the general setup, whereas the lower part shows more detailed side and top views of the liquid fuel burner.

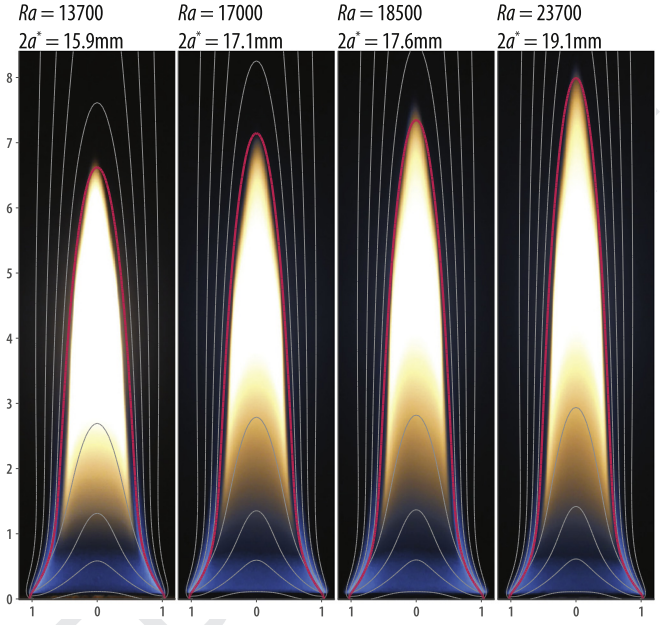

Fig. 6. Steady subcritical heptane flames for different pool diameters (brass wall). Superposed on the photographs are numerical computations following the simplified description given in Section 2; the thick red line indicates the flame front, and the thin gray lines indicate equispaced isotherms $T = 2, 3, 4, 5$. Note that, in order to match the experimental conditions, the vaporizing fuel surface in the numerical computations is set at $x = -0.75\,\mathrm{mm}/a^*$. (For interpretation of the references to color in this figure legend, the reader is referred to the web version of this article.)

interchangeable titanium or brass plate, and the porous layer form a large flush surface. The fuel holder is connected to an external fuel tank with a cross-sectional area of approximately $350\,\mathrm{cm}^2 \gg \pi a^{*2}$. In this manner, once the height of the tank is adjusted so that the burner is filled to the desired level with fuel, this level remains essentially constant during the course of an experiment (typically about ten minutes). To avoid uncontrolled fuel spilling, a very small vertical offset of 0.75 ± 0.25 mm is maintained in the experiments between the fuel-surface level and the rim of the surrounding solid wall.

To prevent external perturbations to the flame, the complete experiment is enclosed by a $3\,\mathrm{m} \times 2\,\mathrm{m} \times 2\,\mathrm{m}$ chamber. After closing the chamber and waiting approximately 10 min for all air currents to die out, the experiment is started. To ignite the fuel remotely, a surface ignitor mounted on a motorized arm was slowly brought close to the fuel and then retracted. The flame dynamics were recorded with a Panasonic Lumix FZ300 camera at a frame rate of 120 fps. For unstable flames, the puffing frequency can be determined from the image sequence by selecting a slice of the image near the flame half-height and computing the power spectral density of the temporal evolution of the average intensity in that region. The period for analysis was typically taken to be one minute, containing about 600 puffing cycles at the expected puffing frequency of 10 Hz. In addition to visible light photographs, shadowgraph images were taken by placing a 3 W led light source in the focal point of a convex lens, situated 150 cm in front of the flame, and projecting the image onto a white paper screen 70 cm behind the flame.

4.2. Experimental results and comparisons for subcritical flames

As expected, steady flames were found for sufficiently small pool diameters. Figure 6 shows photographs of such steady flames over heptane fuel pools of diameter $2a^* = 15.6$, 17.1, 17.6, and 19.1 mm ($Ra = 13{,}700$, $17{,}000$, $18{,}500$, and $23{,}700$). Dimensionless length scales are used in the axes, so that $r = 1$ corresponds to the rim of the fuel pool. Superposed on the photographs are steady numerical computations following the simplified description given in Section 2. The thick red line indicates the predicted flame-sheet location, and the thin gray lines are equispaced isotherms. The computations assume an isothermal wall, appropriate for the brass wall employed. Initial computations for the canonical isothermal-wall problem having the fuel level flush with the horizontal wall produced flame heights appreciably larger than those measured, but, recognizing the experimental necessity of maintaining the fuel level below that of the rim, revised numerical computations were performed with the vaporizing fuel surface set at $x = -0.75\,\mathrm{mm}/a^*$, providing the comparisons shown in the figure. Given the number of approximations involved in the mathematical formulation of the problem, the degree of agreement of the computations with the experimental visualizations, including variations of the predicted shape of the flames with increasing Rayleigh numbers, seems truly remarkable. It is perhaps surprising that the computations reveal such a strong sensitivity to the offset

UNCORRECTED

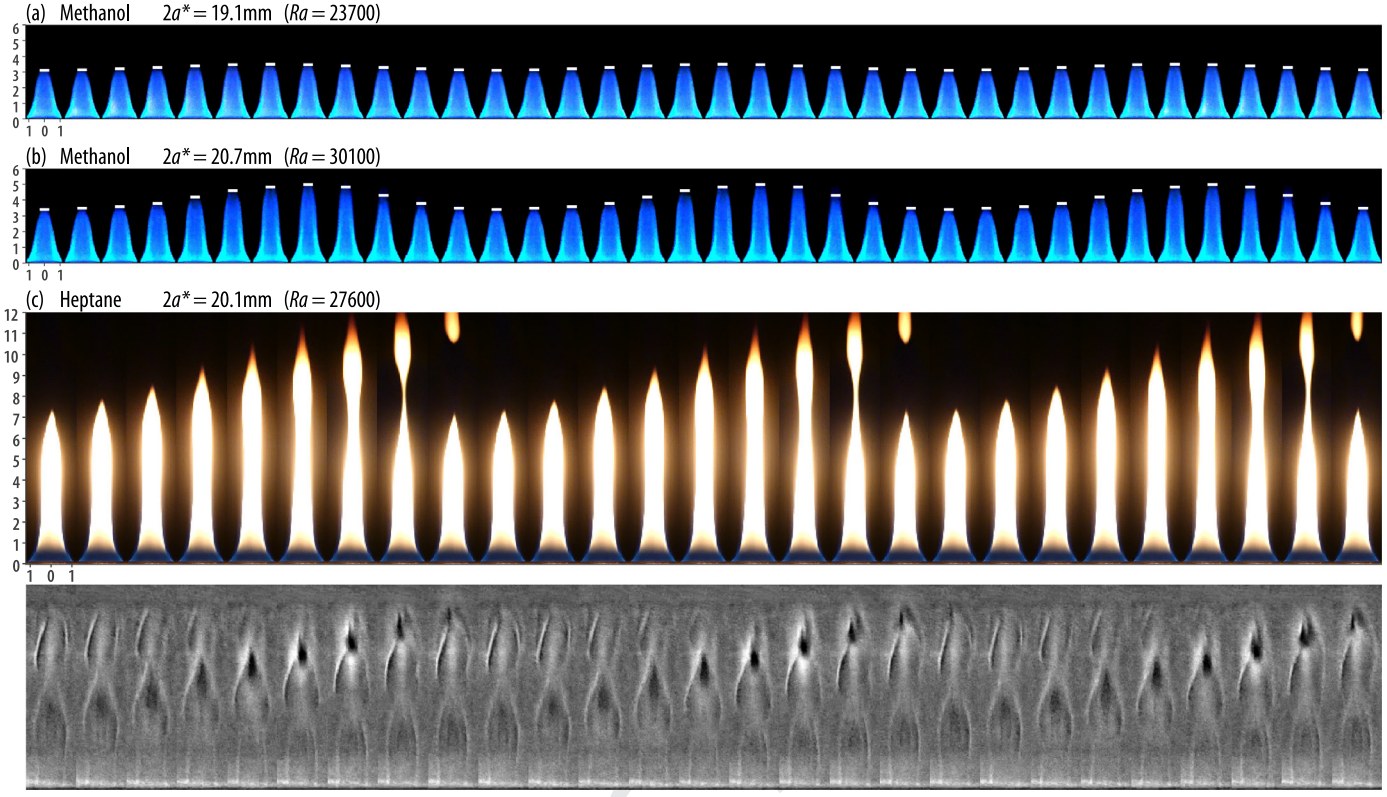

Fig. 7. Three puffing cycles for supercritical (a, b) methanol (titanium wall), and (c) heptane (brass wall) flames. In the first two visible sequences, artificially imposed horizontal bars are marked at the top of the flame to track the flame-height oscillations. Panel (c) is accompanied by a shadowgraph sequence (note that the latter does not correspond to the exact same puffing events as its visible-light counterpart and that the length scales are different). The time interval between the images is 1/120 s. The measured puffing frequencies are (a) $f^* = 10.1$ Hz ($St = 0.0034$), (b) $f^* = 10.0$ Hz ($St = 0.0031$), and (c) $f^* = 12.8$ Hz ($St = 0.0041$).

distance between the fuel level and the horizontal plate; this sensitivity, being larger than sensitivities to other parameters, emphasizes the desirability for thorough care in reporting experimental measurements.

Similar measurements and computations were made for subcritical methanol flames. Although the degree of comparison shown in the figure for heptane was not pursued for methanol, it was observed both experimentally and computationally that methanol flames are less sensitive to the offset distance. This reduced sensitivity likely is associated with the shorter near-critical flame heights for methanol, to be addressed in the following subsection.

4.3. Experimental results and comparisons for supercritical flames

For methanol pool fires that exceed the critical Rayleigh number, the flame is observed to start puffing with a small amplitude, which grows gradually as the diameter of the fuel pool is increased, as shown in Fig. 7a. The critical Rayleigh number for methanol is larger than that for heptane (Fig. 4). From a theoretical point of view, although the temperature of methanol flames is calculated to be generally higher, as dictated by the larger values of q/S, their reduced size, associated with the lower values of S and Le_F, causes them to be more stable than their heptane counterparts, leading one to expect the more mild pulsations observed. The variations shown in the first two sequences of the figure indicate nearly sinusoidal flame-height variations (with amplitudes that increase with increasing Rayleigh numbers).

When the heptane fuel pool diameter is increased to $2a^* = 20.1$ mm ($Ra = 27{,}600$), the steady character of the flow is lost more abruptly, and the flame starts puffing in a periodic manner. Figure 7c shows three oscillation cycles, the top panel with visible-light photographs and the bottom in shadowgraph images. The shadowgraphs show the large vortical structures that characterize the flame envelope; because of the manner in which the shadowgraph images were obtained, an accurate vertical scale for that sequence cannot be defined, but the flame height of the preceding sequence corresponds approximately to the first narrow pinch-off position in the shadowgraphs. These shadowgraph images are in qualitative agreement with the eigenmodes near criticality, obtained from the global stability analysis. A quantitative comparison is not appropriate because of the large oscillation amplitudes seen in Fig. 7c; at $Ra = 27{,}600$ nonlinear effects already play a role in the flow dynamics. The shadowgraph images confirm that the perturbation wavelength is comparable with the flame height, further emphasizing the need for a global stability analysis that takes into account this intrinsic nonparallelism of the flow field.

According to the experimental findings, the critical Rayleigh number for heptane flames using a brass surface surrounding the fuel pool, and under the other specific experimental conditions considered here, lies between that corresponding to the last stable flame, $2a^* = 19.1$ mm, or $Ra = 23{,}700$, and that corresponding to the first puffing flame, $2a^* = 20.1$ mm, or $Ra = 27{,}600$. Decreasing the thermal conductivity of the wall in contact with the base of the flame by changing the brass plate surrounding the fuel pool to a titanium plate decreases the critical Rayleigh number, as indicated in Fig. 4, where the experimental results are given as the last entry of each of the four triplets. These experimental results exhibit approximate agreement when compared with predictions of the canonical cases studied with the global stability analysis, given as the first of each three entries. However, some specific details of the experimental setup are not fully taken into account in the canonical computations, as indicated above; in particular, the

UNCORRECTED PROOF

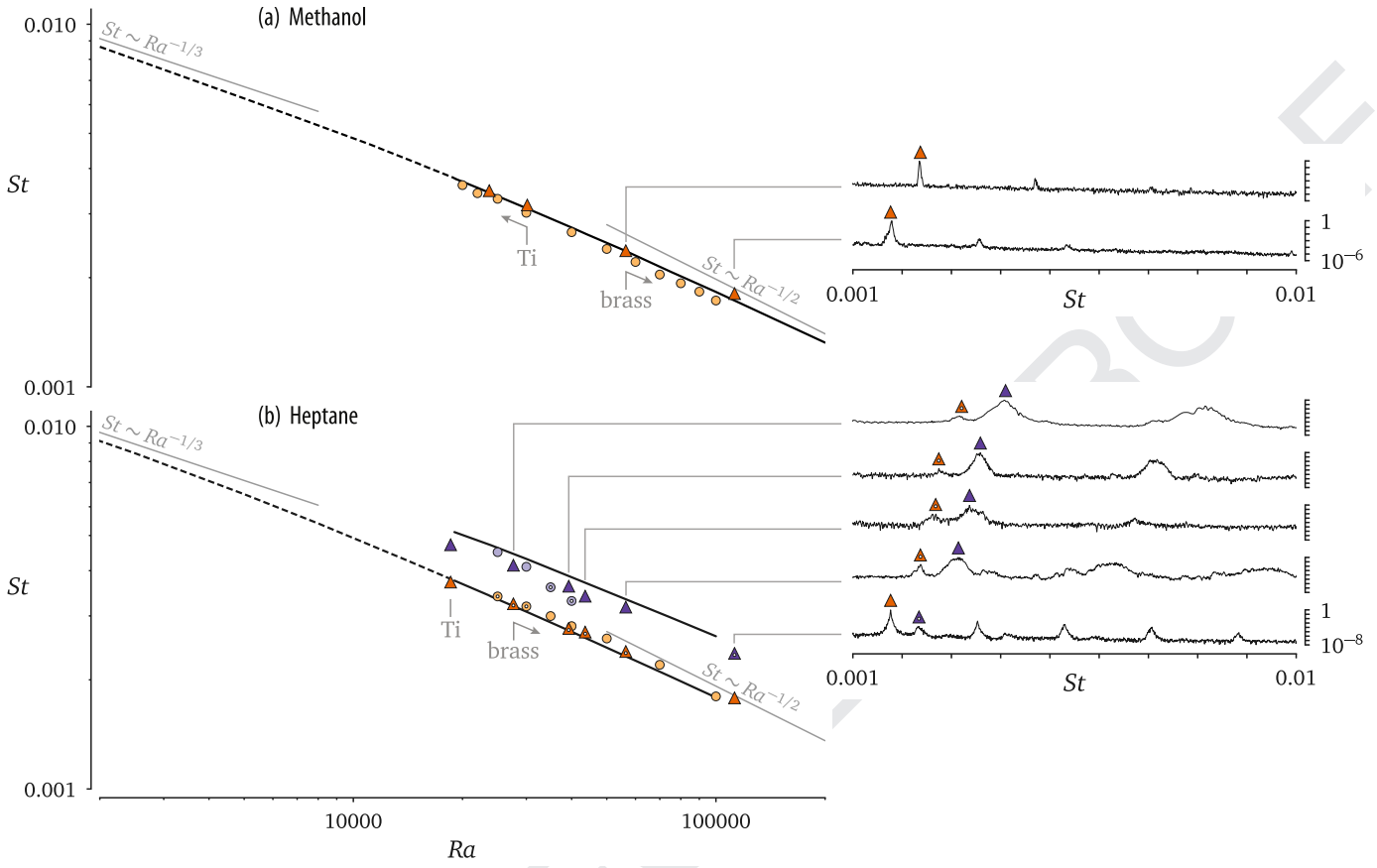

Fig. 8. Dimensionless puffing frequency as a function of the Rayleigh number. Triangles correspond to experimental results; circles are computed from time-dependent direct numerical simulations of the governing equations. The results of the global stability analysis, using (a) adiabatic, and (b) isothermal boundary conditions, are shown as a solid line in the unstable regime and a dashed line in the stable regime. The experimental data points obtained with a brass plate are accompanied on the right-hand side by plots of the power spectral density.

necessary small offset between the fuel level and the rim of the surrounding plate in the experiments has a considerable influence on the stability margins. This was assessed in the global stability analysis by introducing a small offset of the fuel level in the computational domains, 0.75 mm, producing a quantitative change in the global-stability predictions of the onset, listed as the second of each triplet of entries in Fig. 4. The effect on the prediction is seen to be significant, the offset critical values occurring at appreciably larger Rayleigh numbers. In all four cases, the experimentally determined range of the critical Rayleigh number extends into the range between the flush and offset predictions. Only for methanol with the brass plate might the experimental critical Rayleigh number exceed the offset prediction, while for heptane with the brass plate the experimental result definitely lies between the two predictions.

5. Puffing frequency

5.1. Additional measurements

To investigate the dependence of the puffing dynamics and its characteristic frequencies (Strouhal numbers) on the size of the fuel pool, additional experiments were conducted for supercritical diameters up to 32.1 mm ($Ra = 112{,}500$), for both methanol and heptane, with both brass and titanium plates. Results are summarized in Fig. 8. In analyzing the results, it is worth recalling that puffing pool fires are known to be periodic phenomena, such that the entire flow field oscillates at a single frequency [9]. Consequently, the expectation is that the Fourier spectrum of the time signal of any physical quantity should contain one distinguished peak at that frequency. In the figure, besides showing the dependence of the Strouhal number on the Rayleigh number at the left, the measured frequency spectrum is shown at the right.

5.2. Results for methanol

The right-hand side of Fig. 8a shows the normalized power spectral density of the visible light intensity recorded over a rectangular region positioned around the flame half-height, for unstable brass-plate methanol flames with two different diameters (Rayleigh numbers). As expected, for methanol the spectrum is seen to be characterized by a single low-frequency peak and its harmonics. Values of the associated Strouhal number for different $Ra > Ra_c$ are represented as triangles on the left-hand-side plot of Fig. 8a, the four points corresponding to measurements with the titanium plates of two different diameters and with the brass plates of two different diameters, in each case the smaller of the two diameters being that of the unstable point in Fig. 4. These four points show how the frequency decreases with increasing pool size. The error in the frequency measurement was estimated to be less than 0.75 Hz, which was the largest observed variation in the measured puffing frequency over different one-minute intervals, yielding error bars in Fig. 8 that are smaller than the symbols.

The frequencies measured experimentally are compared with predictions of the linear global stability analysis for the canonical case of a pool fire surrounded by an adiabatic wall, represented as black lines on the left plots of Fig. 8a. As discussed in Section 3.3, for methanol the spectrum is dominated by an isolated eigenmode

Please cite this article as: D. Moreno-Boza et al., On the critical conditions for pool-fire puffing, Combustion and Flame (2018), https://doi.org/10.1016/j.combustflame.2018.02.011

(see Fig. 2a), the second most important mode having a growth rate that is much smaller. This is consistent with the purely harmonic behavior observed in the experiments. The predicted and measured values of the frequency for increasing values of *Ra* show excellent agreement, which extends for values of *Ra* well beyond the critical value, in the parametric region where the flow oscillations can be expected to be fully nonlinear. For methanol there is very little difference between measurements with titanium and brass and between computations with adiabatic and isothermal walls.

5.3. Results for heptane

A similar analysis was performed for heptane flames, with results represented in Fig. 8b. Consistent with the previously indicated unexpected importance of two eigenmodes, the spectral content of the signals includes in this case two peaks (together with their harmonics), whose relative intensity varies with *Ra*. On the right it is seen that near the bifurcation the high-frequency mode is dominant, whereas for large fuel pools the low-frequency becomes the most energetic. Both peaks are represented by triangles in the frequency diagram on the left of the figure, with a dot indicating the weaker one. The comparisons on the left plot include also the predictions of the stability analysis. As discussed earlier, for heptane flames the spectrum contains a second relevant eigenvalue, of higher frequency and comparable growth rate. The variation with *Ra* of the Strouhal numbers for these two modes is included as the black lines on the left-hand-side plot of Fig. 8b. The comparison with the experimental results indicates that the two eigenmodes identified in the stability analysis are related to the two distinguished peaks in the experimental spectrum.

5.4. DNS confirmation

The theoretical and experimental results were supplemented with time-dependent direct numerical simulations (DNS) of the differential equations, using the numerical code presented in [45]. This code employs as space discretization a local anisotropic h-adaptive algorithm in a finite-element framework. The finite-element spaces are the same as those employed in the steady computations, described before (quadratic finite elements for coupling functions and velocity, and linear finite elements for pressure). For the time-discretization scheme, a semi-Lagrange-Galerkin method in combination with a second-order BDF scheme is used. The semi-Lagrange–Galerkin method treats the convective terms in a stable way, and decouples the momentum and mass conservation equations from the conservation equations for the coupling functions Z, $\tilde{Z}$ and ξ. Moreover, this time discretization has the ability to transform the nonlinear momentum and mass conservation equations into a linear Stokes problem, which is solved with a preconditioned conjugate gradient Uzawa algorithm. The equations for the coupling functions Z, $\tilde{Z}$, and ξ are solved with a fixed-point iteration to treat the weak nonlinearity induced by the nonunity Lewis number and the dependence of the density and diffusion coefficients on Z, $\tilde{Z}$, and ξ.

The frequency analysis of the DNS results was similar to that employed in connection with the experiments, i.e. the power spectral density of the temporal evolution of the axial velocity in a few points of the flow field was computed. For methanol flames, a single peak was identified, with a frequency that agrees well with the experimental and stability results (circles in Fig. 8a). For heptane flames, however, two different frequencies were distinguished for conditions sufficiently close to the bifurcation. These two frequencies are represented by circles in Fig. 8b, with a dot indicating the weaker one, yielding good agreement with results of the experiments and the global stability analysis. For sufficiently large Rayleigh numbers, the DNS computations did not reveal the presence of a higher-frequency mode. This seems to be consistent qualitatively with the fact that in the experiments the strength of this mode is seen to decay as the Rayleigh number increases.

5.5. Stable regimes and scalings

In the stable regime there are no oscillations of the flame. Nevertheless, the calculated frequency of the least stable of the eigenmodes resulting from the global stability analysis (which is exhibited as dashed lines in Fig. 8) may provide physical insight in the context of small-amplitude harmonic forcing, since the response of the flow may be expected to correspond to a resonance with this stable leading eigenvalue of the spectrum. The frequency of that eigenmode is the frequency at which such a forcing is most efficient, yielding the largest gain in kinetic energy of the flow field [36], this being the nascent eigenmode that becomes unstable when the critical Rayleigh number is reached.

The growth and frequency-selection mechanisms governing the global instability of buoyant diffusion flames act primarily in the flame envelope characterized by large density and velocity gradients [30]. Therefore, on theoretical grounds, a scaling law for the frequency associated with the instability can be derived from a balance between the unsteady and convective terms in the momentum equation, i.e. $f^* \sim V^*/L^*$, where $V^* \sim (g^* L^*)^{1/2}$ is the velocity induced by buoyant acceleration of the flow, and L^* is the characteristic size of this region. For sufficiently large fuel pools, L^* is typically on the order of the pool size a^*, and consequently $f^* \sim g^{*1/2} a^{*-1/2}$. For smaller fuel pools on the contrary, buoyancy starts entering the problem at a distance $L^* \sim \nu_A^{*2/3} g^{*-1/3}$, larger than a^*, leading to $f^* \sim g^{*2/3} \nu_A^{*-1/3}$. From the definition of the Strouhal number, these regimes can be seen to correspond to the scaling laws $St \sim Ra^{-1/2}$ and $St \sim Ra^{-1/3}$, respectively. The resulting dependences are indicated in Fig. 8 by the gray trend lines. It can be seen that these tendencies are recovered by the global stability analysis for the limits of small/large Rayleigh numbers, thereby supporting the scaling estimates.

6. Conclusions

Through all three fundamental classes of scientific methods—theoretical, computational, and experimental—by focusing on methanol and heptane as fuels, this investigation develops information in support of the conclusion that puffing of axisymmetric pool fires in air begins when an appropriately defined Rayleigh number exceeds a critical value. That value, which depends on the thermochemical and transport properties of the fuel and on aspects of the physical configuration, such as the type of material employed for the horizontal surface surrounding the round pool and the vertical offset of the fuel level in the pool, always exceeds unity, being greater than 10,000 if transport properties are evaluated at ambient temperatures but more than 100 times less than that if they are evaluated at the flame temperature. Increasing the vertical offset between the fuel level and its surroundings noticeably increases the value of the critical Rayleigh number for onset of the instability. For the two fuels studied, as with most other fuels as well, the critical Rayleigh number, proportional to the cube of the pool diameter, corresponds to a critical pool diameter of about 20 mm in the laboratory, with an onset puffing frequency on the order of 10 Hz.

Global stability analyses are central to achievement of understanding of the conditions under which puffing occurs and of the oscillatory characteristics of the supercritical puffing modes. To make accurate stability predictions, it is necessary to first obtain accurate predictions of the steady subcritical flames, properly accounting for the configuration and fuel properties. Moreover, in

UNCORRECTED PROOF

Please cite this article as: D. Moreno-Boza et al., On the critical conditions for pool-fire puffing, Combustion and Flame (2018), https://doi.org/10.1016/j.combustflame.2018.02.011

describing the linear stability modes, even though the flames are tall and narrow, parallel-flow approximations are inaccurate, biglobal analyses being required, with two-dimensional eigenfunctions, because the vertical extents of the eigenfunctions are comparable with the flame height. Although one-dimensional eigenfunctions are much simpler to implement computationally, two-dimensional eigenfunctions are needed in these problems.

In most global stability analyses, as critical conditions are approached, only one eigenmode controls the onset of instability, the others being sufficiently stable to be ignored. That is, indeed, found to be true for methanol, but, quite surprisingly, it is concluded here that for heptane two eigenmodes have to be considered, both of them affecting the computed and experimentally observed near-critical puffing frequencies. This unexpected finding is a consequence of the near-critical heptane flame, having a smaller fuel diffusion coefficient, being appreciably taller than the methanol flame, leading to a more prominent Hopf bifurcation. The supercritical methanol instability begins sinusoidally, the amplitude of its flame-height oscillations increasing with an increasing Rayleigh number, but the heptane flame-height oscillation is non-sinusoidal from the beginning, its dominant frequency initially being that of the unstable eigenmode having the higher of the two unstable-mode Rayleigh numbers, and farther along, at higher Rayleigh numbers, becoming dominated by the lower of the two unstable-mode Rayleigh numbers, with DNS computations no longer producing the higher frequency. This more complex heptane behavior may be expected also to occur for fuels whose molecules are larger than heptane, leading to smaller diffusion coefficients.

At large Rayleigh numbers, the appropriate characteristic length, to be employed with the acceleration of gravity in defining a relevant Strouhal number for the dominant frequency of oscillation, is the diameter (or radius) of the pool. That selection results in a scaling in which the Strouhal number decreases with increasing Rayleigh number in proportion to its $-1/2$ power. At small Rayleigh numbers, the appropriate characteristic length for a relevant Strouhal number is larger than the pool diameter and must be constructed from a molecular diffusivity and the gravitational acceleration. In the resulting scaling law, the Strouhal number decreases with increasing Rayleigh number in proportion to its $-1/3$ power. If stable flames are perturbed, they may be expected to respond with natural frequencies determined by the frequency of the least stable eigenmode. The global stability analysis yields eigenmodes that approach these two limits of scaling at large and small Rayleigh numbers.

At Rayleigh numbers considerably larger than those considered in the present work, a secondary instability sets in near the edge of the fuel pool in the form of vortex rolls that are oriented in the streamwise direction, often referred to in the literature as 'finger-like instabilities' or 'toe vortices' [8,10,46]. These structures, which are similar to the vortex instabilities encountered in flow over (nearly) horizontal hot plates [47], may result from the amplification of disturbances in the convectively unstable boundary layer [48] near the pool edge. Although the characteristic length scale of these toe vortices—the boundary-layer thickness at the position they emerge—is much smaller than the pool diameter that characterizes the globally unstable puffing behavior, the two instabilities may interact through large-scale puffing-induced fluctuations of the outer velocity field that is seen by the boundary layer, an aspect which merits further exploration.

A framework has been laid for investigating the occurrence, frequencies, and general characteristics of near-critical, pool-fire puffing phenomena. Although focused on methanol and heptane pools in earthbound laboratories, the nondimensional formulations apply to other environments as well. It would be of interest to explore further how successful these descriptions are, for example through experiments and computations with other liquid fuels.

Acknowledgments

We would like to thank Lorenzo Van Muñoz for his help in the experimental campaign.

References

[1] K.C. Smyth, J.E. Harrington, E.L. Johnsson, W.M. Pitts, Greatly enhanced soot scattering in flickering CH_4/air diffusion flames, Combust. Flame 95 (1993) 229–239.
[2] M. Sibulkin, A.G. Hansen, Experimental study of flame spreading over a horizontal fuel surface, Combust. Sci. Technol. 10 (1975) 85–92.
[3] M.A. Finney, J.D. Cohen, J.M. Forthofer, S.S. McAllister, M.J. Gollner, D.J. Gorham, K. Saito, N.K. Akafuah, B.A. Adam, J.D. English, Role of buoyant flame dynamics in wildfire spread, Proc. Natl. Acad. Sci. USA 112 (32) (2015) 9833–9838.
[4] V.I. Blinov, G.N. Khudyakov, Diffusion burning of liquids, Technical report T-1490a-c, Izdatel'stvo Akademii Nauk SSSR, Moscow, 1961.
[5] M. Hertzberg, K. Cashdollar, C. Litton, D. Burgess, The diffusion flame in free convection: buoyancy-induced flows, oscillations, radiative balance, and large-scale limiting rates, Technical report 8263, Department of the Interior, Bureau of Mines, 1978.
[6] E. Zukoski, B. Cetegen, T. Kubota, Visible structure of buoyant diffusion flames, Symp. (Int.) Combust. 20 (1984) 361–366.
[7] A. Schönbucher, W. Brötz, C. Balluff, G. Riedel, A. Kettler, N. Schiess, Visualization of organized structures in buoyant diffusion flames, Ber. Bunsenges. Phys. Chem. 89 (6) (1985) 595–603.
[8] E.J. Weckman, A. Sobiesiak, The oscillatory behaviour of medium-scale pool fires, Symp. (Int.) Combust. 22 (1988) 1299–1310.
[9] A. Hamins, J.C. Yang, T. Kashiwagi, An experimental investigation of the pulsation frequency of flames, Symp. (Int.) Combust. 24 (1992) 1695–1702.
[10] B.M. Cetegen, T.A. Ahmed, Experiments on the periodic instability of buoyanty plumes and pool fires, Combust. Flame 93 (1993) 157–184.
[11] T. Yuan, D. Durox, E. Villermaux, An analogue study for flame flickering, Exp. Fluids 17 (5) (1994) 337–349.
[12] W.M.G. Malalasekera, H.K. Versteeg, K. Gilchrist, A review of research and an experimental study on the pulsation of buoyant diffusion flames and pool fires, Fire Mater. 20 (1996) 261–271.
[13] J.M. Most, P. Mandin, J. Chen, P. Joulain, D. Durox, A.C. Fernández-Pello, Influence of gravity and pressure on pool fire-type diffusion flames, Symp. (Int.) Combust. 26 (1996) 1311–1317.
[14] A.F. Ghoniem, I. Lakkis, M. Soteriou, Numerical simulation of the dynamics of large fire plumes and the phenomenon of puffing, Symp. (Int.) Combust. 26 (1996) 1531–1539.
[15] W.E. Mell, K.B. McGrattan, H. Baum, Numerical simulation of combustion in fire plumes, Symp. (Int.) Combust. 26 (1996) 1523–1530.
[16] S.R. Tieszen, V.F. Nicolette, L.A. Gritzo, J.K. Holen, D. Murray, J.L. Moya, Vortical structures in pool fires: observation, speculation, and simulation, Technical report SAND96-2607, Sandia National Laboratories, 1996.
[17] K. Prasad, C. Li, K. Kailasanath, C. Ndubizu, R. Ananth, P.A. Tatem, Numerical modelling of methanol liquid pool fires, Combust. Theor. Model. 3 (1999) 743–768.
[18] Y.L. Sinai, Exploratory CFD modelling of pool fire instabilities without cross-wind, Fire Safety J. 35 (2000) 51–61.
[19] T.G. Ma, J.G. Quintiere, Numerical simulation of axisymmetric fire plumes: accuracy and limitations, Fire Safety J. 38 (5) (2003) 467–492.
[20] P. Chatterjee, Y. Wang, K.V. Meredith, S.B. Dorofeev, Application of a subgrid soot-radiation model in the numerical simulation of a heptane pool fire, Proc. Combust. Inst 35 (3) (2015) 2573–2580.
[21] G.M. Byram, R.M. Nelson, The modeling of pulsating fires, Fire Technol. 6 (2) (1970) 102–110.
[22] R.I. Emori, K. Saito, A study of scaling laws in pool and crib fires, Combust. Sci. Technol. 31 (5–6) (1983) 217–231.
[23] P.J. Pagni, Pool fire vortex shedding frequencies, Appl. Mech. Rev. 43 (8) (1990) 153–170.
[24] M.A. Delichatsios, Gravitational fluctuations in pool fires and pool buoyant flows, Combust. Sci. Technol. 112 (1996) 355–358.
[25] J. de Ris, Mechanism of buoyant turbulent diffusion flames, Proc. Eng. 62 (2013) 13–27.
[26] H.W. Emmons, Scientific progress on fire, Annu. Rev. Fluid Mech. 12 (1980) 223–236.
[27] G. Heskestad, Dynamics of the fire plume, Philos. Trans. R. Soc. A 356 (1748) (1998) 2815–2833.
[28] P. Joulain, The behavior of pool fires: state of the art and new insights, Symp. (Int.) Combust. 27 (1998) 2691–2706.
[29] S.R. Tieszen, On the fluid mechanics of fires, Annu. Rev. Fluid Mech. 33 (2001) 67–92.
[30] D. Moreno-Boza, W. Coenen, A. Sevilla, J. Carpio, A.L. Sánchez, A. Liñan, Diffusion-flame flickering as a hydrodynamic global mode, J. Fluid Mech. 798 (2016) 997–1014.
[31] E. Sher, A theoretical study of the combustion of liquids at a free surface, Combust. Flame. 47 (1982) 109–128.
[32] K. Akita, T. Yumoto, Heat transfer in small pools and rates of burning of liquid methanol, Symp. (Int.) Combust. 10 (1965) 943–948.

UNCORRECTED PROOF

Please cite this article as: D. Moreno-Boza et al., On the critical conditions for pool-fire puffing, Combustion and Flame (2018), https://doi.org/10.1016/j.combustflame.2018.02.011

[33] H.W. Emmons, Some observations on pool burning, in: W.G. Berl (Ed.), International Symposium on the Use of Models in Fire Research, National Academy of Sciences—National Research Counsel (1961), pp. 50–67.
[34] A. Liñán, M. Vera, A.L. Sánchez, Ignition, liftoff, and extinction of gaseous diffusion flames, Annu. Rev. Fluid Mech. 47 (2015) 293–314.
[35] A. Liñán, D. Martínez-Ruiz, M. Vera, A.L. Sánchez, The large-activation-energy analysis of extinction of counterflow diffusion flames with non-unity lewis numbers of the fuel, Combust. Flame 175 (2016) 91–106.
[36] W. Coenen, L. Lesshafft, X. Garnaud, A. Sevilla, Global instability of low-density jets, J. Fluid Mech. 820 (2017) 187–207.
[37] K.K. Bharadwaj, D. Das, Global instability analysis and experiments on buoyant plumes, J. Fluid Mech. 822 (2017) 97–145.
[38] R.V.K. Chakravarthy, L. Lesshafft, P. Huerre, Global instability of buoyant jets and plumes, J. Fluid Mech. 835 (2018) 654–673.
[39] X. Garnaud, L. Lesshafft, P.J. Schmid, P. Huerre, Modal and transient dynamics of jet flows, Phys. Fluids 25 (2013) 044103.
[40] F. Hecht, New development in FreeFem++, J. Numer. Math. 20 (3–4) (2012).
[41] W. Schneider, Flow induced by jets and plumes, J. Fluid Mech. 108 (1981) 55–65.
[42] A. Lingens, M. Reeker, M. Schreiber, Instability of buoyant diffusion flames, Exp. Fluids 20 (1996a) 241–248.
[43] A. Lingens, K. Neemann, J. Meyer, M. Schreiber, Instability of diffusion flames, Symp. (Int.) Combust. 26 (1996b) 1053–1061.
[44] R.B. Lehoucq, D.C. Sorensen, C. Yang, Arpack users guide: Solution of large scale eigenvalue problems by implicitly restarted Arnoldi methods, 1997.
[45] J. Carpio, J.L. Prieto, M. Vera, A local anisotropic adaptive algorithm for the solution of low-Mach transient combustion problems, J. Comput. Phys. 306 (2016) 19–42.
[46] P.E. DesJardin, T.J. O'Hern, S.R. Tieszen, Large eddy simulation and experimental measurements of the near-field of a large turbulent helium plume, Phys. Fluids 16 (6) (2004) 1866–1883.
[47] P. Rajamanickam, W. Coenen, A.L. Sánchez, Non-Boussinesq stability analysis of natural-convection gaseous flow on inclined hot plates, Int. J. Heat Mass Transf. 109 (2017) 949–957.
[48] J.F. Clarke, N. Riley, Free convection and the burning of a horizontal fuel surface, J. Fluid Mech. 76 (1976) 415–431.

UNCORRECTED PROOF

Please cite this article as: D. Moreno-Boza et al., On the critical conditions for pool-fire puffing, Combustion and Flame (2018), https://doi.org/10.1016/j.combustflame.2018.02.011